# Journal of Materials Chemistry A

Accepted Manuscript


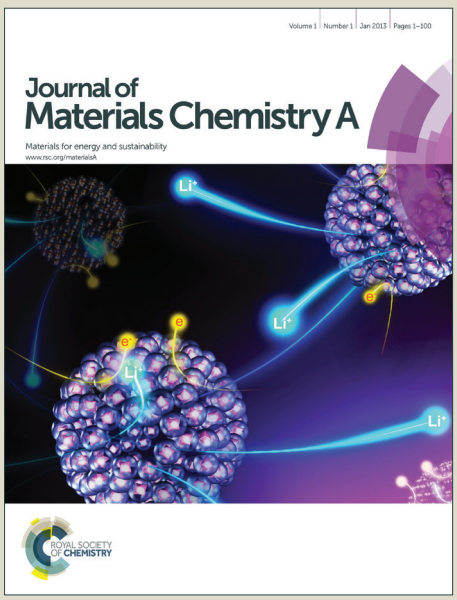





ROYAL SOCIETY OF CHEMISTRY

www.rsc.org/materialsA

Journal Name

RSCPublishing

ARTICLE

# Combinatorial Aerosol Assisted Chemical Vapour Deposition of A Photocatalytic Mixed $SnO_2$/ $TiO_2$ Thin Film

Nicholas Chadwick,[a] Sanjayan Sathasivam,[b] Andreas Kafizas,[a] Salem M. Bawaked,[c] Abdullah Y. Obaid,[c] Shaeel Al-Thabaiti,[c] Sulaiman N. Basahel,[c] Ivan P. Parkin[a] and Claire J. Carmalt[a]*

Cite this: DOI: 10.1039/x0xx00000x

Received 00th January 2012,
Accepted 00th January 2012

DOI: 10.1039/x0xx00000x

www.rsc.org/

Combinatorial Aerosol Assisted Chemical Vapour Deposition (cAACVD) was used to grow a thin film that graduated across its width from tin dioxide to titanium dioxide. This is a relatively new technique that can be used to create a variety of mixed phase and composition thin films on a single substrate. Here cAACVD was used to deposit a mixed phase $TiO_2$ and $SnO_2$ film and composition was related to UV photocatalysis, hydrophobicity and microstructure not inherent to anatase $TiO_2$ or cassiterite $SnO_2$. Characterisation was achieved using X-ray diffraction (XRD), X-ray photoelectron spectroscopy (XPS), scanning electron microscopy (SEM), energy dispersive X-ray spectroscopy (EDX) and UV-Vis spectroscopy. Functional testing to elucidate the differences in functional properties across the film was undertaken by the photo-induced degradation of a resazurin 'intelligent' ink, a photo-induced wettability study and two-point resistivity measurements. Functional properties showed enhanced photocatalysis in comparison to Pilkington Activ™ with similar formal quantum yield (molecules destroyed per absorbed photon) and formal quantum efficiency (molecules destroyed per incident photon) values.

## 1 Introduction

Titanium dioxide is a well characterised and investigated photocatalyst.[1,2,3] Since Fujishima's initial discovery of the ability of titanium dioxide to carry out semiconductor photocatalysis at the boundary between its surface and another medium[4] it has enjoyed prolific investigation within the scientific literature for uses ranging from photovoltaic cells[5] to coatings for the purification of water.[6,7,8] The use of titanium dioxide in these devices can be attributed to its favourable solar mechanics with its band gap lying at 3.2 eV facilitating interaction with UV light. This interaction and absorption of light promotes excited photoelectrons to the conduction band and leaves an electron hole in the valence band which migrate to the surface and undergo surface redox reactions, usually radical based in nature.[9] Titanium dioxide however has two disadvantages that limit its use as an environmental photocatalyst. It suffers from efficient recombination processes limiting the available amount of charged species for use in surface redox reactions[10] and its solar absorption spectrum allows it to interact with only the UV portion of the suns solar radiation. This is then attenuated to between 4-0.5% by the Earth's atmosphere and cloud cover.[11] By doping titanium dioxide it is anticipated that these inadequacies can be overcome by promoting the lifetime of photo-generated electrons and electron holes, hence reducing recombination, and shifting its band gap towards the visible spectrum.[12]

Combinatorial aerosol assisted chemical vapour deposition (cAACVD) is a relatively new field of experimental investigation that conveys many advantages and to the authors' knowledge only one paper has been previously published on the subject.[13] AACVD itself is a low energy atmospheric pressure deposition method which has been used to deposit a wide range of materials from photocatalysts to transparent conducting oxides and super-hydrophobic coatings.[14,15,16,17,18] Therefore, it is a technologically relevant synthetic method for thin film growth which could be easily scaled up in an industrial process.[19] By conducting the deposition in a combinatorial manner, which involves mixing two independent precursor steams within the reactor itself, a film of graded composition can be grown. This allows

differences in microstructure, crystal structure and any resultant functional properties that occur as a result of changes in dopant concentration to be investigated across the width and length of the film in a single experiment.[20] (Figure 1).

Ponja *et al* recently published work detailing the production of a highly photocatalytic, hydrophobic $TiO_2$ and $SnO_2$ mixed thin film via a one pot AACVD synthesis.[21] Photocatalysis was found to be better than an industry standard, Pilkington Activ$^{TM}$, by an order of magnitude. This was attributed to the $Sn^{4+}$ doped $TiO_2$ bulk and tin rich surface which acts as a photoelectron sink. Thus, a combination of enhanced charge separation from within the bulk and surface electron retention was thought to be responsible for the enhanced photocatalysis. The surface morphology was also thought to contribute to the increased photocatalysis due to high surface area. Thus, to study the tin-titanium-oxide system and gain an insight into the growth profile of the photocatalytic phase a combinatorial aerosol assisted CVD study was undertaken to deposit compositional gradients within the Sn–Ti–O system.

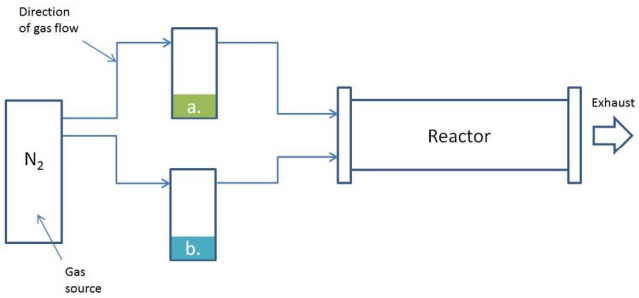


Figure 1: A typical cAACVD setup. A $N_2$ gas source is split between flasks a. and b. which contain different metal oxide precursors which combine only once within the reactor.

## 2 Experimental

### Thin film Preparation using AACVD

Nitrogen (99.99%) (BOC) was used as supplied. Depositions were obtained on $SiO_2$ coated float-glass. Prior to use the glass substrates were cleaned using water, isopropanol and acetone and dried in air. Glass substrates of ca. 90 mm x 45 mm x 4 mm were used. The precursors, titanium tetra-iso-propoxide (99%) and tin butyl tri-chloride (99%) were obtained from Sigma-Aldrich Chemical Co. and used as supplied. Aerosols were generated in ethyl acetate (99%) and carried into the reactor in a stream of nitrogen gas through a brass baffle to obtain a laminar flow. A graphite block, containing a Whatmann cartridge heater, was used to heat the glass substrate. The temperature of the substrate was monitored using a Pt–Rh thermocouple. Depositions were carried out by heating the horizontal bed reactor to the required temperature of 450 $^{o}$C before diverting the nitrogen line through the aerosol and hence to the reactor. The total time for the deposition process took between 20 and 25 minutes. At the end of the deposition, under the nitrogen flow, the glass substrate was left to cool to room temperature with the graphite block before it was removed. To synthesise the combinatorial $TiO_2/SnO_2$ film titanium tetra-iso-propoxide (0.5 g) was dissolved in ethyl acetate (20 ml) and added to a flask. In a separate flask was added tin butyl trichloride (0.5 g) dissolved in ethyl acetate (20 ml) and the separate flasks connected to a split nitrogen line with the aerosol feed leading from the individual flasks to a specially constructed baffle ensuring mixing of titanium and tin precursors happened in the reactor under nitrogen flow. AACVD was carried out at 450 $^{o}$C until both aerosol solutions were exhausted; effort was made to match the intensity of the aerosol so that this happened at roughly the same time.

### Sample Characterisation

X-ray diffraction (XRD) was carried out using a Lynx-Eye Bruker X-ray diffractometer with a mono-chromated Cu Kα (1.5406 Å) source. X-ray photoelectron spectroscopy (XPS) was carried out using a Thermo Scientifiic K-Alpha instrument with monochromatic Al-Kα source to identify the oxidation state and chemical constituents. High resolution scans were done for the Ti (3d), Sn (3d), O (1s) and C (1s) at a pass energy of 40 eV. The peaks were modelled using Casa XPS software with binding energies adjusted to adventitious carbon (284.5 eV). SEM images were taken on a JOEL JSM-6301F Field Emission instrument with acceleration voltage of 5 kV. Images were captured using SEMAfore software. Samples were cut into coupons representing the locations on the grid and coated with a fine layer of gold to avoid charging. The optical transmission was measured over 350–1500 nm range using a Lamda 950 UV/Vis spectrometer.

### Functional Property Testing

Photocatalytic activity was assessed using an established method based on a resazurin 'intelligent ink' first developed by Mills *et al.*[22] Photo induced wettability was tested by placing the samples under a UVC lamp for 2 hours then measuring the water contact angle by placing a 5 µL droplet onto the surface of the films. The film was then irradiated overnight for 16 hours and water contact angles were re-measured. Water droplet contact angles were measured using a First Ten angstroms 1000 device with a side mounted rapid fire camera after casting a 5 µL droplet from a fixed height onto the surface. To assess the photocatalytic activity of the film at sites marked at specific grid positions the whole sample was first washed with water, rinsed with isopropanol and irradiated for 30 minutes to clean and activate the sample. A resazurin based ink was then evenly applied using a spray gun and the photo-induced degradation of the resazurin ink monitored by canning whole images of the film and calculating the photo activity by measuring the change in the red component of the pixels of the scanned images at specific grid positions.[23] Formal quantum efficiency (FQE) and the formal quantum yield (FQY) was then calculated. Formal

quantum efficiency was calculated by dividing the rate of dye molecules destroyed per s per $cm^2$ by the photon flux (4.53 x $10^{14}$ photons per $cm^2$ per s). The formal quantum yield was calculated by dividing the rate of dye molecules destroyed per s per $cm^2$ by the number of photons absorbed by the films. The photon flux and photon absorption for each film was determined using a UVX digital radiometer with a detector for 365 nm radiation attached.

**Preparation of 'intelligent ink' solution**

Glycerol (99.6%), hydroxy ethyl cellulose [average Mv ¼ 90 000], resazurin (92%) were all purchased from Sigma-Aldrich Chemical Co. and used as supplied. The 'intelligent' ink consisted of resazurin (40 mg) redox dye in an aqueous solution (40 mL) with glycerol (3 g) and hydroxylethyl cellulose (0.45 g) that was aged for 24 hours at 3–5 $^0$C. The solution was mixed thoroughly before use.

## 3 Results and Discussion

A mixed phase $TiO_2$/$SnO_2$ thin film was grown by cAACVD. The deposition of $TiO_2$ and $SnO_2$ in ethyl acetate, which acted both as an oxygen source and a carrier medium was achieved using different flasks ensuring that mixing of the two precursors occurred only once inside the reactor. This was done to provide a film whose composition transitioned from $SnO_2$ to mixed phases in the middle through to $TiO_2$ on the other side. The film was characterised by a range of techniques including XRD, XPS, SEM, EDX and UV-Vis spectroscopy. Specifically, characterisation was carried out on twenty individual areas which comprised a grid which allowed the mapping of the entire film, shown in Figure 2. Functional testing in the form of photocatalysis, water contact angle measurement and resistivity measurements were carried out to map the change in functional properties across the film as the composition of $TiO_2$ and $SnO_2$ changed across the width and length of the film.

## Characterisation

**XRD**

X-ray diffraction patterns for a selection of individual spots present on the grid, shown in Figure 2, were obtained. It is evident that distinct regions of different crystal structures and composition exist across the length and width of the film. Therefore the film exhibits crystal phase change vertically as well as horizontally. Without any in depth analysis XRD confirms that the deposition of separate areas of anatase $TiO_2$ and cassiterite $SnO_2$, with mixed phases in between, has been successfully achieved. $SnO_2$ was observed to be present on the left hand side of the film, dominating the lower left hand region of the film with $TiO_2$ occupying the whole length of the right hand side and a mixed $TiO_2$/ $SnO_2$ phase deposited in the top left hand corner (see supporting material).

Figure 2 shows the crystal structure transitions to these mixed phases from the $SnO_2$ and $TiO_2$ regions respectively. The combinatorial nature of the film is evident throughout the rest of the XRD patterns as areas of cassiterite $SnO_2$ change to anatase $TiO_2$ from the left of the film to the right of the film, with mixed areas apparent in the central region

It is clear that along the length of column **A**, where the $SnO_2$ precursor is introduced into the reactor through to the exhaust, the XRD pattern changes from cassiterite $SnO_2$ (grid positions **A1**, **A2** and **A3**) to both $TiO_2$ and $SnO_2$ (grid position **A4**). **A1** exhibits characteristic {110}, {101}, {200}, {211} and {220} crystal planes associated with cassiterite $SnO_2$. The difference between grid positions **A1-3** and **A4** is that {110} and {211} cassiterite planes are observed without the {101} cassiterite plane. In addition, crystal planes associated with anatase $TiO_2$, specifically the {101} and {105} planes were then observed.

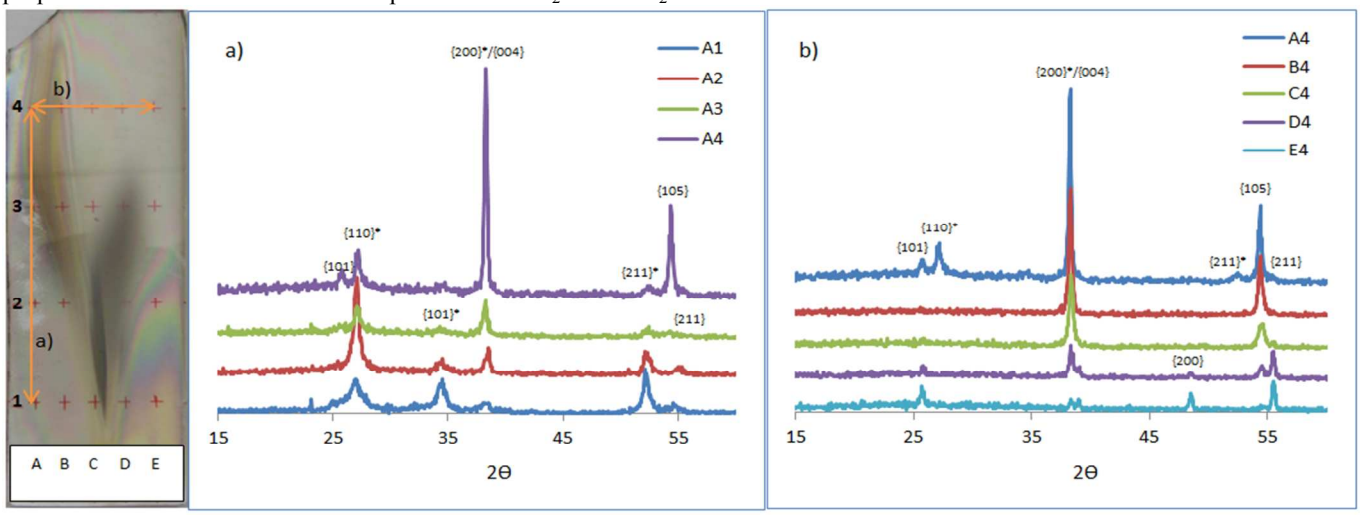


Figure 2: As seen on the film, graph a) corresponds to an overlay of XRD patterns for positions 1-4 along column **A** and graph b) corresponds to XRD for position **A-E** across row **4**. Crystal phases denoted * correspond to cassiterite $SnO_2$ all others are anatase $TiO_2$. a) Moving from row one to four in column **A** the phase transitions from cassiterite to a mixed phase. b) As focus progresses from left to right along row **4** a transition from the mixed phase to **E4** is observed with suspected anatase phases with specific preferred orientation present at the **B** and **C** positions, and standard anatase at the **D** and **E** positions.

The {200} plane also increases in intensity in **A4** compared to **A1** and this is thought to be due to overlap with the {004} plane observed in anatase $TiO_2$ XRD patterns in other grid positions (Figure 2a).

Across row four, from **A4** to **E4** (Figure 2b), the XRD pattern changes from the mixed phase described above (grid position **A4**) to another mixed phase (grid positions **B4** and **C4**) almost identical to **A4** but lacking the {101} anatase $TiO_2$ and {110} cassiterite $SnO_2$ peaks. Specifically, they exhibit the {200} and {105} planes of both cassiterite and anatase respectively. However, since these XRD patterns represent the transition from grid positions **E4** / **D4** (anatase $TiO_2$) through to **A4** (mixed $SnO_2/TiO_2$) it is thought that the {004} anatase plane and the {200} cassiterite plane overlap to give the enhanced intensity of the peak observed in **B4** and **C4**.

A Le Bail refined model was used to investigate the degree of lattice expansion exhibited by the mixed phase areas found at **A4**, **B4**, **C4**, **D4** and **E4**, as shown in Table 1.

Table 1: Le bail refinement of XRD patterns for row **4** shows overall an increase in the anatase unit cell volume and the cassiterite unit cell volume concordantly decreases as the film progresses from E4 to A4.

| Sample | Dep. Temp ./ °C | Phase(s) | a/Å | c/Å | Unit cell Volume/ Å$^3$ | Volume Expansion/ % |
|---|---|---|---|---|---|---|
| $TiO_2$ | - | anatase | 3.784 | 9.514 | 136.268 | - |
| $SnO_2$ | - | cassiterite | 4.738 | 3.187 | 71.552 | - |
| A4 | 450 | anatase | 3.834 | 9.413 | 138.423 | 1.58 |
| | | cassiterite | 4.662 | 3.145 | 68.366 | -4.44 |
| B4 | 450 | anatase | 3.782 | 9.557 | 136.756 | 0.35 |
| | | cassiterite | 4.749 | 3.180 | 71.762 | 0.29 |
| C4 | 450 | anatase | 3.775 | 9.588 | 136.639 | 0.25 |
| | | cassiterite | 4.793 | 3.144 | 72.241 | 0.96 |
| D4 | 450 | anatase | 3.769 | 9.603 | 136.436 | 0.12 |
| | | cassiterite | 4.749 | 3.183 | 71.799 | 0.34 |
| E4 | 450 | amorphous | | | | |

It is evident that overall the anatase unit cell volume increases from **E4** to **A4** suggesting a change from pristine $TiO_2$ to Sn-doped $TiO_2$ at **A4**. The cassiterite unit cell volume decreases overall from **E4** through to **A4** which suggests a transition from pure cassiterite $SnO_2$ to Ti-doped $SnO_2$. Compared to previously reported $TiO_2/SnO_2$ composite films it appears that **A4** exhibits a marked increase in unit cell volume for anatase but, contrastingly, a large decrease in cassiterite unit cell volume (see Table 1). This suggests substitutional doping of $Sn^{4+}$ (ionic radii 0.69 Å) into the $TiO_2$ lattice and substitutional doping of Ti (crystal radii 0.75 Å) for Sn atoms (crystal radii 0.83 Å) in the $SnO_2$ lattice causing an increase and decrease in volume respectively.

XRD of the grid position immediately next to **A4**, specifically **B4**, exhibits a mixed $SnO_2/TiO_2$ region with preferred orientation in the {200} and {105} planes for $SnO_2$ and $TiO_2$ respectively. Le Bail refinement of this crystal phase shows that the $TiO_2$ {004} plane overlaps the $SnO_2$ {200} plane, resulting in enhanced intensity of the peak. As we transition from **B4** to **A4** except for the {101} and {110} planes now being present, the diffraction pattern remains largely unchanged in comparison to **A4**. This supports the idea of insertion of tin as an interstitial dopant which can be attributed to the growth of the monoliths observed in the SEM (Figure 6) at **A4**.

## XPS

X-ray Photoelectron Spectroscopy (XPS) depth profiling was carried out for the 20 grid positions of the film. At each spot a surface scan was taken and then the film was sputtered for 100s after which another scan was taken. This process was repeated four times to provide a concentration profile of titanium relative to tin that represented both the surface of the film and the material in the bulk.

Both Sn and Ti exhibit +4 oxidation states in the bulk and on the surface and match well with literature values (458.3 eV, 463.9 eV for $TiO_2$ and 486.5 eV, 494.9 eV for $SnO_2$). The surface was observed to be relatively tin rich at positions lying to the left of the centre of the film (positions **A1-2** and **B1-2**), which is where the Sn precursor aerosol enters the reactor (Figure 3). A similar situation arises to the right of the centre of the film with the surface being Ti rich, as this is where the titanium precursor aerosol enters the reactor. It is noteworthy that the **A4** position exhibits a slightly lower Sn ratio compared to its surroundings. This could be due to the difference in crystal structure described above or a result of differing surface morphology. Along column **A**, the surface was observed to be tin rich at **A1** through to **A4** but decreasing in intensity relative to titanium. Overall the surface is relatively Sn rich but the Ti: Sn ratio increases across the film from left to right, demonstrating again the combinatorial nature of the film found in XRD.

After 100s of sputtering (Figure 4) the left hand side of the film remains tin rich, however **A4** and **B4** have Ti:Sn ratios >1 indicating they are now tin deficient. The combinatorial nature

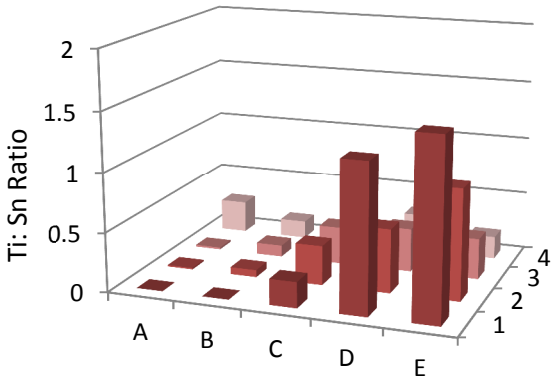


Figure 3: XPS Ti: Sn ratios of all twenty grid positions after 0s of sputtering. The ratio of titanium to tin is seen to increase in a smooth transition from column A to E confirming the combinatorial nature of the film.

of the film remains evident but the Ti: Sn ratio to the right hand side increases indicating that $TiO_2$ is more prevalent in the

bulk. Anomalously, **C4** exhibits, relative to the other grid positions, a relatively high Ti:Sn ratio. Only positions **A-C1** and **A-B2** exhibit Ti:Sn ratios <1 indicating that the positions which are tin rich in nature decrease from the surface towards the bulk. Column **A** mirrors that of the surface with the tin inlet **A1** being tin rich and decreasing in tin concentration through to **A4**.

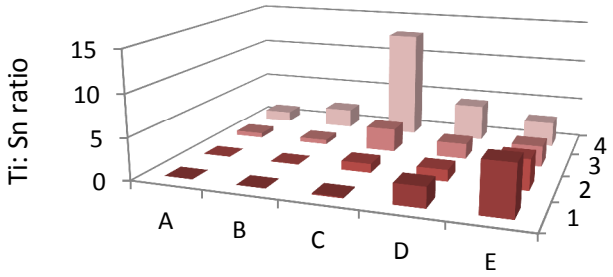


Figure 4: XPS Ti: Sn ratios of all twenty grid positions after 100s of sputtering. The combinatorial nature of the film is therefore evident within the bulk as well as the surface.

After 200s of sputtering the Ti:Sn ratio of the right hand side of the film continues to increase relative to the left hand side which remains tin rich in nature in the same positions as after 100s. The Ti:Sn ratio at positions **A4** and **B4** continues to increase, indicating $TiO_2$ is now the dominant phase present within the bulk. After 300s of sputtering the Ti:Sn ratio continues to increase for all grid positions bar **A-C1** and **A-B2**, which still retain Ti:Sn ratios <1 and thus remain tin rich in nature. After 400s of sputtering the majority of the film exhibits a Ti: Sn ratio >1 sparing grid positions at **A-B1** and **A-B2**, this is not surprising as these sites are situated in the immediate vicinity of where the tin precursor is introduced into the reactor. Column **A** exhibits a similar concentration profile as before but titanium has a more dominant role.

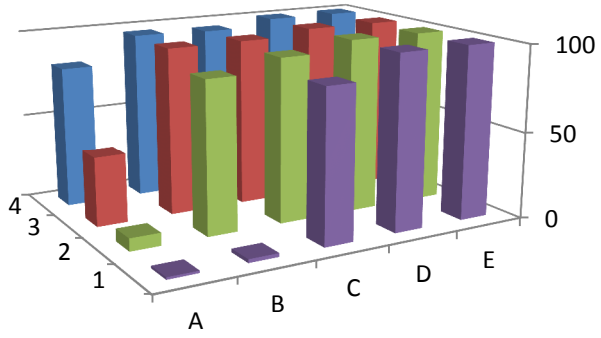


Figure 5: Percentage of titanium relative to tin, measured by EDX, across the entirety of the film. It is evident that titanium dioxide is the majority component of the film but tin concentrations start high in column A and diminish quickly across the rest of the columns.

**EDX**.

Energy dispersive X-ray spectroscopy was used to obtain further insight into the relative ratio of Ti to Sn found throughout the film at specific grid positions. It was observed that titanium dioxide is the dominant phase throughout the majority of the film except in the immediate vicinity of the entry point of the tin precursor at **A1** and **B1** (Figure 5). This agrees with the XPS results, in that $TiO_2$ is dominant in the bulk in all grid positions sparing those found in the immediate vicinity of where the Sn precursor enters the reactor, specifically, **A1** and **B1**.

**SEM**

Scanning Electron microscopy (SEM) was undertaken at all 20 grid positions to provide insight into the surface morphology, which is integral to understand as it plays an important part in photocatalysis.

As shown in Figure 7, across row **1** left to right, the surface morphology changes from that typically observed for cassiterite $SnO_2$[24] to anatase $TiO_2$.[25] Interestingly at **D1**, $TiO_2$ spherical growths can be seen to have formed on top of the original $TiO_2$ morphology and by **E4** the surface appears to have been covered by these spherical growths. Similarly moving left to right across row **2**, cassiterite morphology was exhibited at **A2** and **B2**, before spherical growths similar in nature to those found at **D1** and **E1** were seen on position **C2** and **D2** and granular $TiO_2$ exhibited at **E2**. Row **3** exhibits a granular morphology at **A3** and **B3** before exhibiting cassiterite morphology with spherical growths at **C3**. Standard $TiO_2$ granular morphology was observed at **D3** and **E3**. Row **4** exhibits unique morphology at **A4** similar in nature to photocatalytic $SnO_2/TiO_2$ films previously reported[21] (Figure 6). **B4** exhibits a similar monolithic structure to **A4** but it is not as well defined in nature and the monoliths are smaller in size. The same is true for **C4** with the monolithic growths being even smaller in size and exhibiting a more granular morphology. Surprisingly cassiterite is shown at **D4**, suggesting that

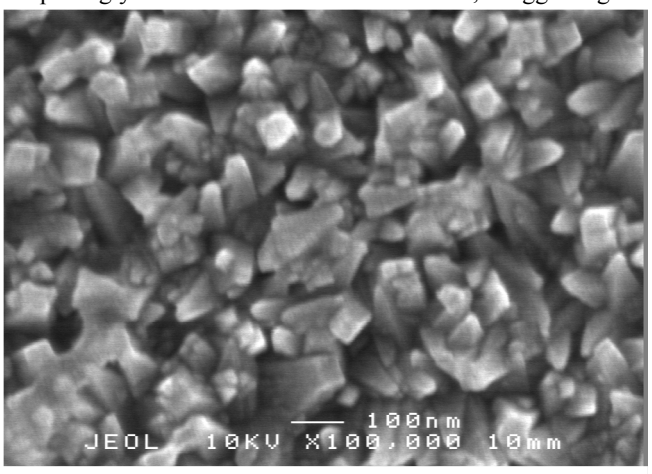


Figure 6: A close up of grid position A4 displaying the monolithic nature of the surface morphology

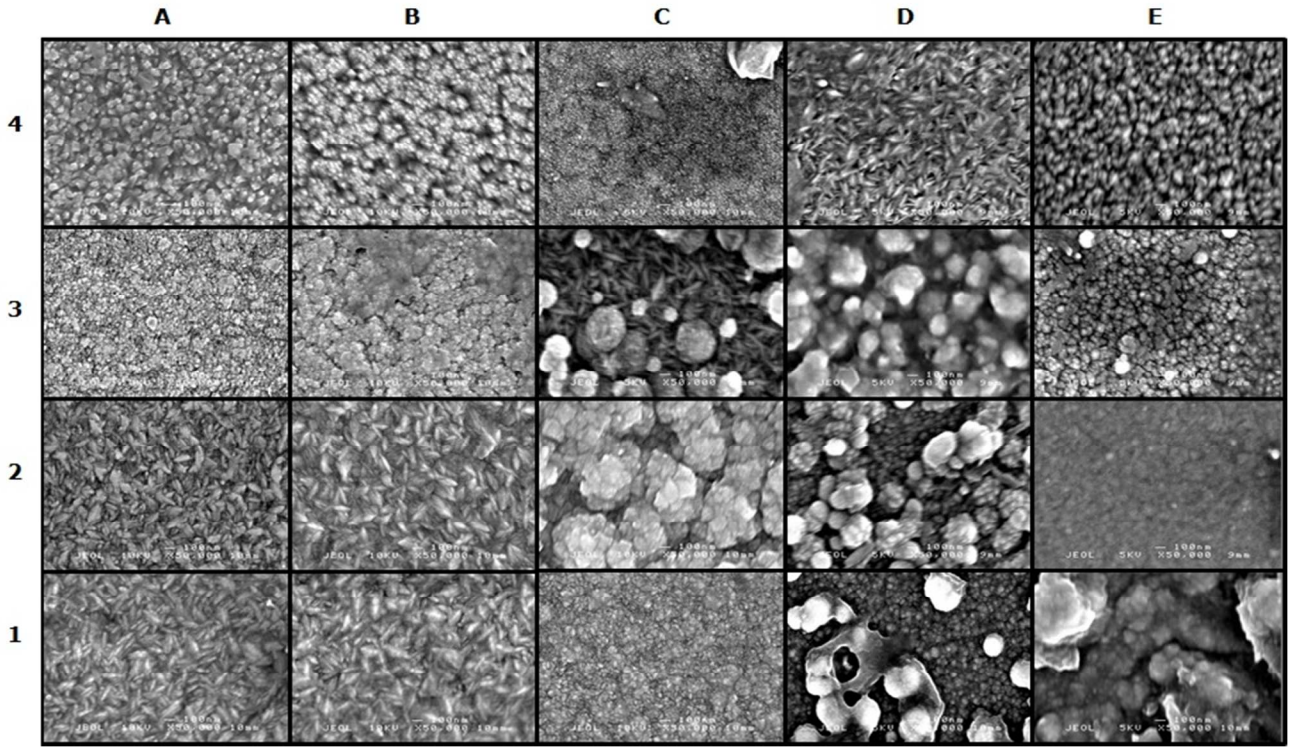


Figure 7: A composite image of all 20 SEMs arranged in a grid. Cassiterite morphology is seen in columns 1 and 2 and anatase morphology seen in columns D and E, intermediate morphology is seen in column C. Of particular interest is the morphology found at A4 which exhibit monolithic growths.

cassiterite has a specific role to play in the growth of the material at **A4**. Finally **E4** exhibits standard $TiO_2$ morphology.

### UV/Vis reflectance data

UV-Visible spectroscopy was carried out at all 20 grid positions and the swanepoel method[26] used to deduce the differences in film thickness across the film. No overall trend in film thickness can be deduced as a result of a transition from $SnO_2$ to $TiO_2$ across columns **A** to **E** but all grid positions exhibit film thicknesses between 90-500 nm which are in line with expected values for previously reported thin films of these materials.[27,28] Transmission and reflectance data for grid position **A4** is shown below (Figure 8).

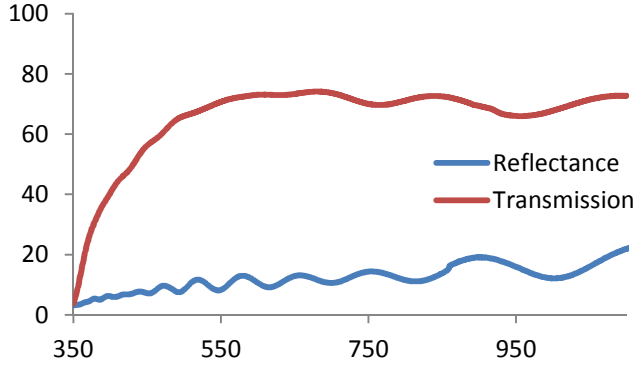


Figure 8: Reflectance and transmission data for grid location **A4**.

### Band Gap

Band gap measurements were obtained from UV-Vis data by Tauc plot analysis to give an idea as to the degree of change in band gap that may occur when mixed phases are produced. It also gives an indication of where cassiterite or anatase is present since the band gap for $SnO_2$ is 3.6 eV[29] and the band gap for $TiO_2$ is 3.2 eV.[30] It can be seen from both indirect (3.12 eV) and direct (3.42 eV) band gap measurements that grid position **A4** exhibits a band gap lower in energy than its surroundings (Figure 9-10). This agrees with previous studies of Sn-doped $TiO_2$ where surface segregated Sn states, like those exhibited at grid position **A4**, were found to lower the band gap of Rutile powders.[31] Overall the band gap appears to increase as

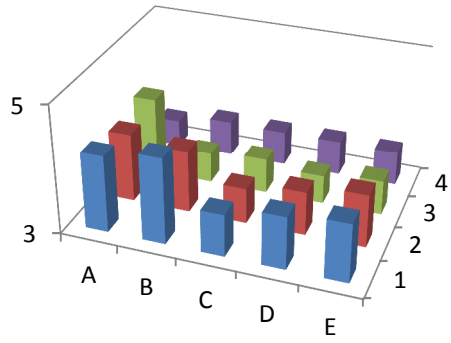


Figure 9: Direct band gap values for all 20 grid positions

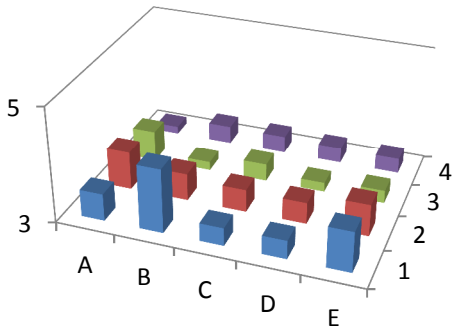


Figure 10: Indirect band gap values for all 20 grid positions. Across both plots a band gap decrease is seen at **A4** relative to its surroundings.

grid positions move away from **A4**, to values ranging between 3-4 eV. However, theroetical studies have shown that substitution of Ti for Sn within anatase $TiO_2$ can have the opposite effect and in fact increase the band gap of $TiO_2$.[32] Hence the position of the tin dopant appears to be responsible for the altering of the observed band gaps between **A4**, where surface segregated Sn is found and has a lower than expected band gap, and the right hand side of the film which is predominantly $TiO_2$ and varies in band gap from 3-4 eV, but exhibits Sn throughout its structure in dopant concentrations, according to XPS.

## Functional testing

### Photocatalysis

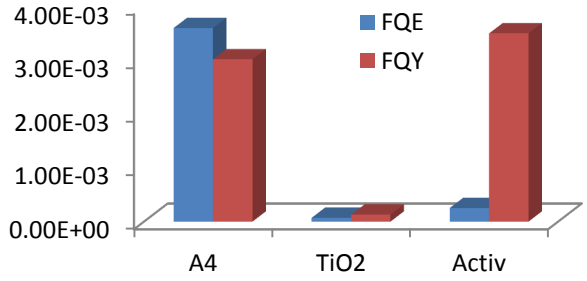


Figure 11: A comparison of FQE and FQY between; grid position A4, $TiO_2$ and an Industry standard, Pilkington Activ™

The combinatorial film was spray coated with an even layer of "Intelligent Ink" first utilised by Mills *et al*.[22] The photo-reduction reaction was induced by UVA light (flux = 4.53 x $10^{14}$ photons per $cm^2$ per s) and monitored by scanned images representing different stages in the degradation process. The photo degradation of the resazurin dye to its pink intermediate occurred fully after roughly 35 minutes at the area of **A4**. It is evident that there is only one area of photocatalytic interest which occurs at the **A4** grid point. The photocatalytic rate for this particular point was determined by measuring the increase in the red component of the digital image pixel that makes up the image at grid position **A4** by using a previously proven method.[23] The photocatalytic rate at **A4** was calculated to be $1.37x10^{12}$ molecules destroyed per $cm^2$ per second, Formal quantum efficiency (FQY) was calculated to be $3.6x10^{-3}$ molecules destroyed per absorbed photon and the formal quantum efficiency (FQE) was calculated to be $3.02x10^{-3}$ molecules destroyed per incident photon. The rest of the film exhibits little photo activity of merit.

Figure 11 compares the observed FQE and FQY for grid position **A4**, $TiO_2$ and commercial glass, Pilkington Activ™, the FQE is an order of magnitude higher but is on par with the FQY.

### Water Contact Angles

Water contact angles were obtained for all 20 grid positions, the sample was then irradiated for 16 hours and the water contact angles were re-measured. The biggest degree of angle change and thus photo-induced wettability was observed in the area identified by the previous dye study as being the most photocatalytic in nature with **A4** exhibiting the biggest change. Interestingly the previously reported hydrophobic property of mixed $TiO_2$ and $SnO_2$ composite materials was not observed at **A4** (Table 2). This is attributed to poor uniformity across the surface morphology.

Table 2: Water contact angles; before and after irradiation, at UV light of wavelength 254nm for all 20 grid locations. The largest change is exhibited by **A4** showing that this is the grid position of highest photo activity.

| Before Irradiation/ ° | | | | | |
|---|---|---|---|---|---|
| | **A** | **B** | **C** | **D** | **E** |
| **1** | 61.04 | 65.13 | 72.28 | 70.76 | 79.92 |
| **2** | 80.28 | 63.67 | 65.29 | 61.94 | 76.28 |
| **3** | 45.23 | 67.13 | 63.1 | 67.71 | 68.91 |
| 4 | 54.52 | 51.79 | 79.07 | 71.09 | 73.61 |
| After Irradiation of 254nm UV for 16 hours/ ° | | | | | |
| | **A** | **B** | **C** | **D** | **E** |
| **1** | 66.32 | 75.78 | 67.8 | 84.39 | 59.24 |
| **2** | 66.13 | 69.44 | 43.06 | 58.19 | 43.77 |
| **3** | 19.28 | 22.02 | 28.93 | 54.09 | 48.45 |
| **4** | 14.64 | 15.18 | 38.08 | 57.03 | 49.78 |

### Two Point Resistance

Two point resistance measurements were taken to provide an empirical idea of relative Sn and Ti areas as $SnO_2$ is a well-known and documented high quality conductor, whereas

titanium dioxide exhibits resistance in the mega ohm region. The difference in resistance between the two materials is several orders of magnitude and thus distinguishing areas of $TiO_2$ and $SnO_2$ should be readily evident. As shown in Table 3, the left hand side of the film exhibits low resistance akin to that of $SnO_2$ in the kilo-ohm region, whereas the right hand side abruptly increases into the mega ohm region and grid positions **D1**, **E1** and **E2** exhibits resistance values higher than 5 x $10^6$ Ohms. This is therefore indicative of $TiO_2$.

Table 3: Two point resistivity measurements (ohms) provide an insight into areas of titanium dioxide and tin dioxide due to the differing degree to which they conduct. High resistivity values indicate $TiO_2$ whereas low resistivity values suggest $SnO_2$.

| | A | B | C | D | E |
|---|---|---|---|---|---|
| 1 | 5.94E+02 | 4.70E+02 | 5.13E+04 | 5.00E+06 | 5.00E+06 |
| 2 | 3.60E+03 | 1.54E+04 | 3.38E+04 | 1.10E+06 | 5.00E+06 |
| 3 | 1.76E+05 | 1.31E+05 | 6.64E+04 | 1.10E+06 | 1.20E+06 |
| 4 | 1.09E+06 | 1.80E+04 | 6.57E+04 | 1.10E+06 | 1.30E+06 |

## 4 Conclusions

Combinatorial aerosol assisted chemical vapour deposition (cAACVD) was carried out at 450 $^oC$ under $N_2$ gas flow using a titanium dioxide precursor (titanium tetra iso-propoxide), a tin dioxide precursor (butyl tin trichloride) and an oxygen source (ethyl acetate). The resultant film, which graduated from $SnO_2$ to $TiO_2$ across the width of the film exhibited intermediate states between cassiterite $SnO_2$ and anatase $TiO_2$ and enhanced photo-activity capable of outperforming an industry standard was found in specific locations. By overlaying a grid, fast and efficient mapping of changes in functional properties and their relation to physical properties across the surface of the film were tracked. Thus we can establish the following:

- XRD, XPS, EDX and SEM demonstrate the graduating nature of the film from $SnO_2$ to $TiO_2$, left to right, across the width of the film.
- XRD and XPS depth profiling showed that, except where the Sn precursor enters the reactor (**A1** and **B1**), all grid locations to the left hand side of the film were anatase $TiO_2$ in the bulk but $SnO_2$ rich at the surface and all grid positions to the right were anatase $TiO_2$. This phenomenon of segregation of $SnO_2$ relative to $TiO_2$ has been reported previously in the literature.[33,34] SEM largely shows the expected morphologies for the respective $SnO_2$ and $TiO_2$ areas found in XRD.
- XPS depth profiling showed the formation of a $SnO_2$ rich surface with a $TiO_2$ phase within the bulk. XRD showed both crystal phases were present at **A4** and Le Bail modelling exhibited a unit cell volume increase in anatase $TiO_2$ and a subsequent unit cell volume decrease in the cassiterite $SnO_2$. This suggests substitutional doping of Sn into the $TiO_2$ matrix and of Ti into the $SnO_2$ matrix.
- The XRD of position **B4** exhibited a mixed $SnO_2$/$TiO_2$ region with preferred orientation in the {200} and {105} planes for $SnO_2$ and $TiO_2$ respectively. Le Bail refinement of this crystal phase showed that the $TiO_2$ crystal plane {004} overlaps the $SnO_2$. Transitioning left from **B4** to **A4**, insertion of the {101} anatase and {110} cassiterite planes was observed, with the diffraction pattern otherwise largely remaining unchanged. This is therefore attributed to the growth of the monoliths observed in the SEM and the enhanced photocatalysis found at **A4**. Whilst it is difficult, due to the data available, to conclusively comment on the growth mechanism for the photocatalytic composite film observed at **A4**, it is thought that the initial formation of titanium dioxide provides a base on which $Sn^{4+}$ doped $TiO_2$ crystal phase grows followed by a Sn rich layer on the surface. Evidence for this was obtained for the tin concentration relative to titanium from XPS and that both cassiterite and anatase phases were observed concurrently in the XRD.
- Functional testing demonstrated that **A4** exhibits the highest degree of photocatalytic activity with a photocatalytic rate of $1.37x10^{12}$ molecules destroyed per $cm^2$ per second with a FQY and FQE of $3.02x10^{-3}$ and $3.6x10^{-3}$ respectively. This compares well with an industry standard, Pilkington Activ$^{TM}$ with a superior photocatalytic rate and FQE, with comparable FQY. This is attributed to the presence of a surface segregated tin layer and tin doped $TiO_2$ within the bulk which cause surface photocatalysis to be superior than Pilkington Activ$^{TM}$. Due to the nature of the grid system used to sample the whole film it is possible that an area of higher photocatalytic activity was not identified. Indeed, although **A4** exhibits superior photocatalytic activity to Pilkington Activ$^{TM}$, it is lower than that observe for composite $SnO_2$/$TiO_2$ films reported previously.[21] This is likely to be due to a lower surface area for **A4** compared to the whole film studied in the previous report caused by less regular or pristine morphology at **A4**. This would reduce the rate of photocatalysis. However, position **A4** demonstrated the greatest degree of photo-induced wettability but exhibited a relatively high resistivity, attributed to poor uniformity of surface morphology. All other grid locations exhibited expected resistivity values for $SnO_2$ and $TiO_2$ respectively. Overall trends for Sn:Ti ratios responsible for the best photocatalytic activity cannot be used as the composite film at **A4** is not a homogenous phase but a supposition of two which exhibits a synergism between $TiO_2$ and $SnO_2$.

We have, to our knowledge, for the first time used combinatorial aerosol assisted chemical vapour deposition to deposit a mixed phase thin film of technological interest. This could have implications in the future for predicting dopant concentrations responsible for the growth and formation of specific phases and tailoring future experiments to enable the growth of higher quality films and the enhancement of previously reported functional properties.

## 5 Acknowledgements

Thank you to Dr Felicity Sartain and Dr Robert G. Palgrave for useful discussions, Mr Kevin Reeves for assistance with SEM imaging and Mr Martin Vickers for XRD assistance. Thank you also to Pilkington NSG for the glass substrates. The project was funded jointly between the UCL Impact scheme and the Deanship of Scientific Research (DSR), King Abdulaziz University, Jeddah under grant no. D-5/432. The authors, therefore, acknowledge UCL and the DSR with thanks for their technical and financial support.

## 6 Notes

*a* Materials Chemistry Research Centre, Department of Chemistry, University College London, 20 Gordon Street, London, U.K. WC1H 0AJ.

*b* Bio Nano Consulting Ltd, 338 Euston Road London, NW1 3BT.

*c* Chemistry Department, King Abdulaziz University, Saudi Arabia

## 7 References

1. A. Fujishima, T. N. Rao, and D. A. Tryk, *J. Photochem. Photobiol. C*, 2000, **1**, 1–21.
2. A. J. Frank, N. Kopidakis, and J. Van De Lagemaat, *Coord. Chem. Rev.*, 2004, **248**, 1165–1179.
3. V. N. Kuznetsov and N. Serpone, *J. Phys. Chem. B*, 2006, **110**, 25203–9.
4. A. Fujishima, *Nature*, 1972, **238**, 37–38.
5. M. Grätzel, *J. Photochem. Photobiol. C Photochem. Rev.*, 2003, **4**, 145–153.
6. P. K. J. Robertson, J. M. C. Robertson, and D. W. Bahnemann, *J. Hazard. Mater.*, 2012, **211-212**, 161–71.
7. J. Blanco-Galvez, P. Fernández-Ibáñez, and S. Malato-Rodríguez, *J. Sol. Energy Eng.*, 2007, **129**, 4.
8. A. Duret and M. Grätzel, *J. Phys. Chem. B*, 2005, **109**, 17184–91.
9. J.-M. Herrmann, *Environ. Sci. Pollut. Res. Int.*, 2012, **19**, 3655–65.
10. J.-M. Herrmann, *Appl. Catal. B Environ.*, 2010, **99**, 461–468.
11. A. N. N. R. Webb, *Photochem. Photobiol.*, 1991, **54**.
12. M. V. Dozzi and E. Selli, *J. Photochem. Photobiol. C Photochem. Rev.*, 2013, **14**, 13–28.
13. C. E. Knapp, A. Kafizas, I. P. Parkin, and C. J. Carmalt, *J. Mater. Chem.*, 2011, **21**, 12644.
14. K. Choy, *Prog. Mater. Sci.*, 2003, **48**, 57–170.
15. X. Hou and K. L. Choy, *Chem. Vap. Depos.*, 2006, **12**, 583–596.
16. N. Noor and I. P. Parkin, *J. Mater. Chem. C*, 2013, **1**, 984.
17. D. S. Bhachu, G. Sankar, and I. P. Parkin, *Chem. Mater.*, 2012, **24**, 4704–4710.
18. C. R. Crick, J. C. Bear, P. Southern, and I. P. Parkin, *J. Mater. Chem. A*, 2013, **1**, 4336.
19. P. Marchand, I. a Hassan, I. P. Parkin, and C. J. Carmalt, *Dalton Trans.*, 2013, **42**, 9406–22.
20. a Kafizas and I. Parkin, *J. Am. Chem. Soc.*, 2011, **133**, 20458.
21. S. Ponja, S. Sathasivam, N. Chadwick, A. Kafizas, S. M. Bawaked, A. Y. Obaid, S. Al-Thabaiti, S. N. Basahel, I. P. Parkin, and C. J. Carmalt, *J. Mater. Chem. A*, 2013, **1**, 6271.
22. A. Mills, J. Wang, S.-K. Lee, and M. Simonsen, *Chem. Commun. (Camb).*, 2005, 2721–3.
23. A. Kafizas, D. Adriaens, A. Mills, and I. P. Parkin, *Phys. Chem. Chem. Phys.*, 2009, **11**, 8367–75.
24. N. Noor and I. P. Parkin, *Thin Solid Films*, 2013, **532**, 26–30.
25. A. A. Tahir, T. a. N. Peiris, and K. G. U. Wijayantha, *Chem. Vap. Depos.*, 2012, **18**, 107–111.
26. R. Swanepoel, *J. Phys. E.*, 1983, **1214**.
27. S. M. Ali, S. T. Hussain, S. A. Bakar, J. Muhammad, and N. U. Rehman, *J. Phys. Conf. Ser.*, 2013, **439**, 012013.
28. J. Yoon, H. K. Oh, and Y. J. Kwag, *J. Korean Phys. Soc.*, 1998, **33**, 699–704.
29. V. B. Kamble and A. M. Umarji, *AIP Adv.*, 2013, **3**, 082120.
30. K. M. Reddy, S. V Manorama, and A. R. Reddy, 2002, **78**, 239–245.
31. F. E. Oropeza, B. Davies, R. G. Palgrave, and R. G. Egdell, *Phys. Chem. Chem. Phys.*, 2011, **13**, 7882–91.
32. R. Long, Y. Dai, and B. Huang, 2009, 650–653.
33. K. K. Akurati, A. Vital, R. Hany, B. Bommer, T. Graule, and M. Winterer, *Int. J. Photoenergy*, 2005, **07**.
34. H.-J. Wang and S.-C. Lee, *Mater. Trans.*, 2009, **50**, 2329–2334.

**Graphical Abstract**

A mixed phase $TiO_2$ and $SnO_2$ film was deposited by combinatorial aerosol assisted chemical vapour deposition was and composition was related to photocatalysis, hydrophobicity and microstructure not inherent to anatase $TiO_2$ or cassiterite $SnO_2$.